https://doi.org/10.1016/j.jmatprotec.2019.03.018
This is the Pre-Published Version.

Effects of grains and twins on deformation of commercial pure titanium in ultraprecision diamond turning

Zejia Zhao[a], Suet To[a,]*, Jingwei Wang[b]

[a]State Key Laboratory of Ultra-precision Machining Technology, Department of Industrial and Systems Engineering, The Hong Kong Polytechnic University, Hung Hom, Kowloon, Hong Kong SAR, China

[b]Shenzhen Key Laboratory of Advanced Materials, Department of Materials Science and Engineering, Shenzhen Graduate School, Harbin Institute of Technology, Shenzhen 518055, China

* Corresponding author. Tel.: +852 2766 6587.
E-mail address: sandy.to@polyu.edu.hk (S. To).

Abstract

This paper theoretically and experimentally analyses and discusses the material deformation mechanism of commercial pure titanium (CP Ti) in ultraprecision machining. One sample with two obviously diverse microstructures is first obtained by compressive test followed by electropulsing treatment (EPT) for 30 s. Then, ultraprecision diamond turning was conducted on the specimen to investigate the effects of grains and twins on the microcrack nucleation and deformation behaviour during cutting process. The results show that microcracks primarily nucleate in large grains and thick twins rather that small grains or twins. Furthermore, critical resolved shear stress (CRSS) and barrier stresses induced by grain or twin boundaries and dislocations are introduced in the proposed model, which not only compares the deformation difference between grains and extension twin of $\{10\bar{1}2\} < 10\bar{1}\bar{1} >$ type, but also simulates the

© 2019. This manuscript version is made available under the CC-BY-NC-ND 4.0 license http://creativecommons.org/licenses/by-nc-nd/4.0/

relationship between resolved shear stresses, cutting shear angles strain rates and temperature for the first time in ultraprecision diamond turning.

Keywords: Commercial pure titanium (CP Ti); Ultraprecision diamond turning; Grains and deformation twins; Microcracks; Critical resolved shear stress (CRSS).

1. Introduction

The superior corrosion resistance and high strength to weight ratio of commercial pure titanium (CP Ti) contribute to its applications in a broad range of biomedical facilities. For instance, Elias et al. (2008) compared mechanical properties of four grades of CP Ti and demonstrated their applications in three types of dental implant: osseointegrated, mini-implant for orthodontic anchorage, and zygomatic. Generally, biomedical replacements require the materials not only to have essential mechanical properties, but also to possess sufficient surface precision and form accuracy in order to satisfy applications on hard tissue substitutions of humans; hence, precision finishing or surface improvement of CP Ti is particular necessary after rough machining. However, Muhammad et al. (2014) reported that the inherent nature of inferior thermal conductivity, chemical reaction at high temperature, and low modulus of elasticity, brings great challenges in machining titanium and its alloys.

Ultraprecision diamond turning is an advanced and efficient technique for manufacturing high precision components with surface roughness at nanometric level and form accuracy in the submicrometric range, and no subsequent finish machining is required, as demonstrated by Cheung and Lee (2000). The effects of material microstructures, such as crystal types, crystalline orientations as well as grain or twin sizes, have been attracting a great amount of attention for several decades in diamond

turning. Furukawa and Moronuki (1988) compared the cutting force variation in polycrystal, single-crystal and amorphous materials. They found that cutting forces vary at grain boundaries in polycrystalline aluminium, while random or smooth cutting forces were observed during cutting single-crystal fluorite and amorphous acrylic resin. Furthermore, material crystallographic orientations greatly affect the cutting forces and surface generation, as claimed by Lee et al. (2013). The atoms in different crystal orientations show various arrangement and periodicity in single crystal materials, contributing to anisotropic behaviour that the physical and chemical features vary with crystal orientations. In polycrystalline materials, random distribution of massive crystal grains give rise to isotropic properties, but according to Rahman et al. (2017), the deformation behaviour of polycrystals is also greatly affected by atom arrangements or crystal structures in ultraprecision diamond turning because of the "grain size effect". In ultraprecision diamond turning, the grain size is comparable to the uncut chip thickness, resulting in a single grain of the workpiece was removed in the direction of cutting depth. Therefore, the flow stresses required to overcome workpiece deformation are affected by the heterogeneity of the polycrystalline materials.

Sahoo et al. (2016) reported that polycrystalline CP Ti shows α phase with hexagonal close packed (hcp) crystalline structure at ambient temperature, and the phase could transform to body centered cubic (bcc) β phase if temperature exceeds 882.5 °C. Sun et al. (2011) claimed five essential deformation systems in deforming of polycrystal hcp materials, and they also pointed out that prismatic <a> slip is prone to be activated among these deformation modes when the c/a ratio is less than 1.633. Basal <a> slip, pyramidal <a> slip and <c+a> slip are the other glide modes in deformation of CP Ti. Furthermore, Xie et al. (2016) proposed that twinning modes of $\{10\bar{1}2\} < 10\bar{1}\bar{1} >$,

$\{11\bar{2}1\} < \bar{1}\bar{1}26 >$ and $\{11\bar{2}2\} < 11\bar{2}\bar{3} >$ and $\{11\bar{2}4\} < 11\bar{2}1 >$ could act as assistant roles to accommodate deformation, and the extension twin of $\{10\bar{1}2\} < 10\bar{1}\bar{1} >$ type (T1 twin) is the earliest and most prevalent twin in comparison to others. The formation of twins in hcp materials was found to be affected by the misorientation angles according to Beyerlein et al. (2011) who pointed out that twins preferentially nucleate and grow at grain boundaries with low misorientation angles. However, the possibility of twin nucleation would be reduced if there are massive twin-twin and slip-twin interactions that are sources of strain hardening in deforming of α-titanium, as demonstrated by Salem et al. (2005). Besides, secondary twins could nucleate between two primary twins, forming a "ladder-like" structure which might restrict dislocation motion and enhance strain hardening according to Allain et al. (2004) and Gumus et al. (2015). Hence, the nucleation of deformation twins could affect the strength and ductility of materials. Qin and Jonas (2014) supposed that the T1 twinning could result in a misorientation angle of about 85° from the direction of $< 10\bar{2}0 >$, and it may also be able to enhance the flow stress of hcp materials. Kaschner et al. (2007) proposed that the generation of twins could also inhibit the dislocation propagation, resulting in a barrier effect on hcp material deformation. Knezevic et al. (2010) reported that the deformation twins could introduce a new orientation that is different from its parent crystal. This phenomenon may affect the ductility of hcp materials, which depends on the activated twin systems.

The activation of different crystal systems depends on the resolved shear stress on slips or twins. If the resultant resolved shear stress exceeds the critical resolved shear stress (CRSS) of one deformation system, a corresponding glide would occur. According to Hutchinson and Barnett (2010), an applied stress to overcome material flow stress is the

synthetic stress of CRSS and hardening stress induced by dislocations and second particles. The CRSS of different slip or twin systems in CP Ti have been widely reported for several decades. Though no consensus has been achieved on the values of CRSS due to different microstructures and chemical content, it is generally accepted that prismatic slip is easier to be activated than other slips or twins. Besides, the hardening stress caused by dislocations is an important factor to influence the flow stress of deformation. Rahman et al. (2017) also modelled the material flow stress by considering the effects of grain boundaries and dislocations in ultra-precision machining. Melkote et al. (2015) pointed that the dislocation motion induced by grain boundaries and dislocation forests could affect the flow stress of CP Ti in machining process.

However, titanium and its alloys are regarded as one of difficult to cut materials due to the low thermal conductivity and inferior elastic modulus according to Arrazola et al. (2009). Microcracks have been usually observed in the machined surface of titanium and its alloys. Sharman et al. (2001) demonstrated that increase in cutting depth could induce a high density of cracks in the turned surface of gamma titanium aluminide alloy. Ulutan and Ozel (2011) reported that the formation of titanium carbide in titanium and nickel alloys might also result in microcracks which are formed by the complete removal of carbide particles. A large number of surface cracks have also been observed in titanium alloy when the cutting tool is no longer sharp according to Priarone et al. (2016). Besides, Shokrani et al. (2016) founded that the absence of flood cooling could contribute to cracks formation on the Ti–6Al–4V titanium alloy during machining. Though some studies have been conducted on investigation of cracks formation on the machined surface, little research was carried out on exploring the effects of grains and twins on nucleation of microcracks in machining process. In addition, investigation of

deformation mechanisms in ultraprecision machining of CP Ti was rarely reported with respect to resulted shear stress and barrier stresses. Therefore, the purpose of this study is to explore the effects of grain sizes and deformation twins on crack nucleation and deformation behaviour in ultraprecision diamond turning of CP Ti.

2. Materials and experimental procedures

The chemical composition of as-received CP Ti (Grade 1) with a diameter 4 mm is tabulated in Table 1. The CP Ti was first wire-cut into samples with a height of 8 mm, half of which were then subjected to compressive deformation with a height reduction ratio of 40%. Next, electropulsing treatment (EPT) on an ETP device was conducted to rapidly anneal the compressed CP Ti, as schematically shown in Fig. 1. The voltage and frequency of EPT was 30 V and 300 Hz, under which conditions the temperature could reach about 450 °C, thereby recrystallization is able to occur in the compressed Ti. After EPT for 30 seconds, the samples were cooled in the air. Finally, a part of as-received samples and compressed samples followed by EPT (CEPTs) were mechanically ground, electrolytically polished, and chemically etched for metallographic observation, while the others were used for ultraprecision diamond turning. The experiment was repeated by three times to ensure reliability.

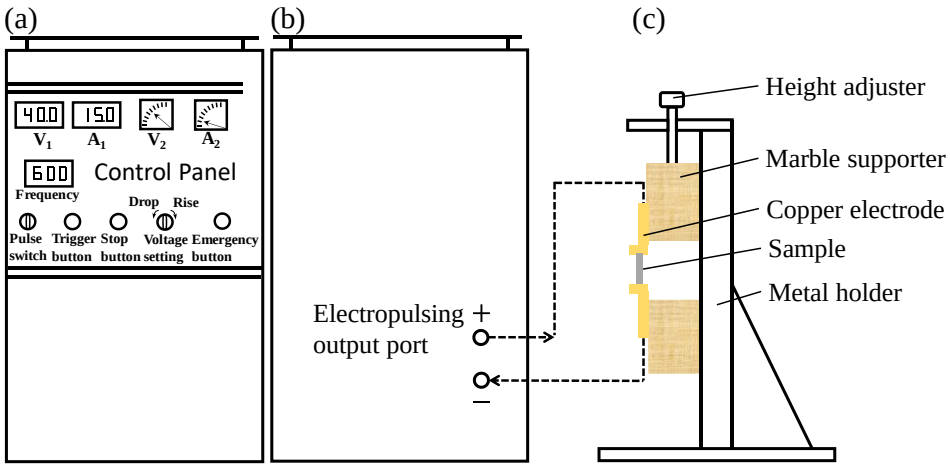

Fig. 1 EPT device of (a) front view, (b) back view and (c) a sample fixture

Table 1 Elements and corresponding contents of the as received CP Ti

Elements	Fe	O	C	N	H	Ti
Content/wt%	0.13	0.10	0.01	0.001	0.001	Bal.

An ultra-precision machine, Moore Nanotech 350FG, was utilized to conduct the diamond turning process. A flat surface was firstly obtained by rough machining process with a spindle speed of 1500 rpm, cutting depth of 4 μm and feed rate of 6 mm/min, and then finish turning of three passes with a spindle speed of 1000 rpm, cutting depth of 3 μm and feed rate of 4 mm/min was carried out with a fresh diamond tool (nose radius: 1.20 mm; rake angle: 0°; front clearance: 12.5°). Under the finish cutting tool, a Kistler 9256C1 force sensor was mounted to measure the turning forces. A DFC 450 optical microscope (LEICA) was used for metallographic observation. The electronic images and electron backscattered diffraction (EBSD) patterns of microstructures were obtained from a Hitachi S4700 scanning electron microscope (SEM) equipped with EBSD measuring system. The surface roughness and three-dimensional (3D) morphologies were measured by a Nexview three-dimension (3D) optical surface profiler (Zygo). The Vikers hardness and Young's modulus of surface were tested by a hardness testing machine (Mitutoyo) with an indentation load of 1 N for 20s and a Nano Indenter G200, respectively.

3. Results and discussion

3.1 Surface morphologies and crystal microstructure

Fig. 2 (a) and (f) schematically show the as-received and CEPT treated CP Ti samples respectively. Two yellow areas are selected as analytical regions for optical microscopy observation, while six small grey areas are chosen for scanning electron microscope

analyses. Optical surface morphologies of the two sets of workpiece after single point diamond turning are shown in Fig. 2 (b) and (c). Obvious turning microcracks are observed on machined surfaces of the as-received and CEPT treated samples. The microcracks in the as-received workpiece are distributed randomly on the whole turning surface, while those in the CEPT treated samples do not appear until the diamond tool passes through the green curve marked in Fig. 2 (c).

The optical microstructures of the two kinds of samples are given in Fig. 2 (d) and (e), corresponding to the as-received and CEPT samples, respectively. The average grain size R of the CP Ti was estimated by the linear intercept method that is proposed by Kusama et al. (2017):

$$R = \frac{3L}{4N} \tag{1}$$

where L is the length of a line segment marked on the OM images and N is the number of grains on the line. The average grain size of the as-received CP Ti is calculated to be about 52 μm. Some randomly distributed twins within grains are also observed from Fig. 2 (d). However, the microstructure of CEPT samples is significantly distinct from that of the original samples, showing two obvious different microstructure zones, as shown in Fig. 2 (c) and (e). Small grains are observed at the outside of workpiece (Zone I: region within the black dash line) due to recrystallization, while large grains and plenty of twins are observed on the right side of workpiece (Zone II). Besides, microcracks are scarcely found in Zone I but are extensively discovered in Zone II, which means that turning microcracks are mostly generated in sites with the large grains or twins.

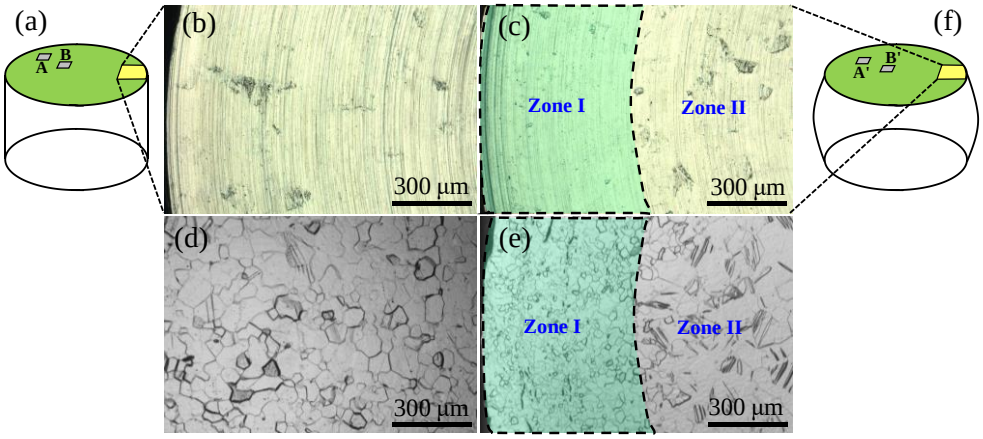

Fig. 2 CP Ti samples of (a) schematic diagram, (b) diamond turned surface morphology and (d) OM microstructure; CEPT treated specimen of (c) turned surface, (e) microstructure and (f) schematic diagram

In order to clarify which factor determines the formation of cracks, some indentation marks in the vicinity of the cracks are made after diamond turning, as shown in Fig. 3. Firstly, most of cracks are formed in the large grains instead of their neighbouring small grains or grains with acicular α phase, as shown in Fig. 3 (a), (b), (f) and (g). Then, it can be seen from Fig. 3 (c) and (h) that some cracks are also observed to form in the twins with rather thick width, but they are not likely to be formed in the thin twins (Fig. 3 (d) and (i)). In addition, the edges of microcracks closely coincide with the large grain or twin boundaries, which substantiates that the boundaries of large grains or twins provide potential sites for the initiation of microcracks. When the diamond cutting tool meets one grain boundary of a potential site, cracks firstly generate at the boundary and terminate as the tool passes through the opposite grain boundary of the large grain or twin, forming shapes that are similar to corresponding grains or twins. Moreover, Fig. 3 (e) and (j) demonstrate that the presence of thin twins in the large grains could restrain the propagation of cracks. Since cracks formed in one grain or twin were not likely to

propagate to its neighbouring small grains or thin twins, intergranular cracks were generated in diamond turning of CP Ti with large size of grains and twins. Fig. 3 (k) schematically summarizes the crack formation in turning of CP titanium with different microstructures. The green and red boundaries represent the initiation and termination of microcracks, respectively.

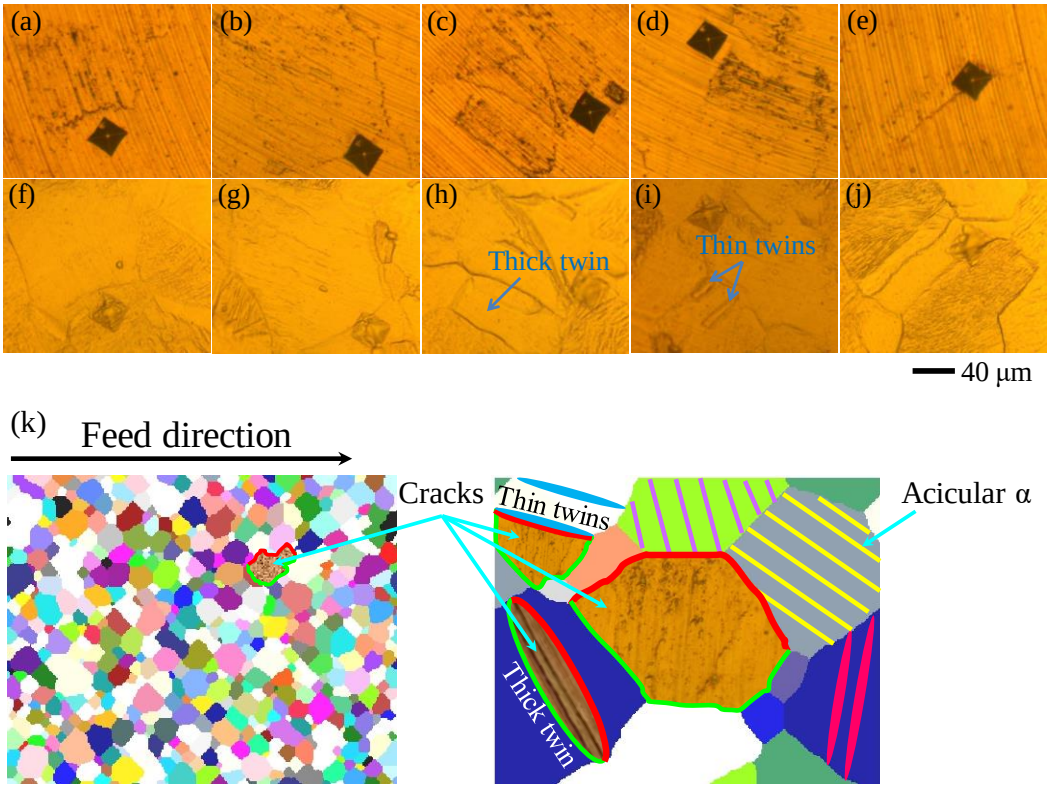

Fig.3 (a) - (e) morphologies of microcracks on turning surface of CEPT treated workpiece; (f) - (j) corresponding microstructures of (a) - (e); and (k) schematics of cracks formation in large grains/twins and a few small grains

Fig. 4 shows the SEM morphologies of diamond turned surfaces of the as-received and CEPT treated workpiece. Similarly, primary cutting microcracks (yellow marks) show casual distribution in the as-received workpiece, but those in the CEPT treated samples occur only in the region with large size of grains and thick deformation twins.

Delamination failure (white circles) can also be observed obviously in these cracks. Furthermore, the formation of microcracks is similar to the generation of cleavage fracture during cutting brittle materials, such as glass, silicon and silicon carbide, so the nucleation of microcracks may be deformed in a brittle mode.

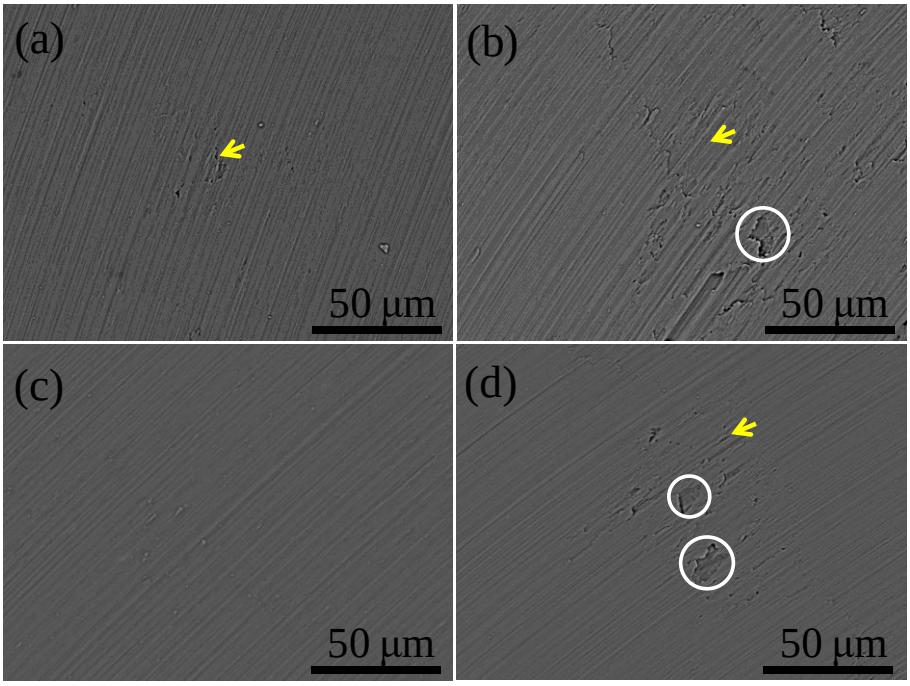

Fig. 4 SEM morphologies selected from regions (a) A, (b) B of CP Ti and (c) A', (d) B' of CEPT samples

Microcracks observed in the SEM morphologies are pits instead of bulges, which could be verified from the 3D Zygo profiles, as illustrated in Fig. 5 (g) and (h). The depth of the microcracks reaches the highest value at the delamination sites in the cracks. As the formation of cracks would deteriorate the surface quality, local area surface roughness in Zone I distributing small grains is the best for the CEPT treated samples, reaching a value of about 31 nm, as shown in Fig. 5 (d).

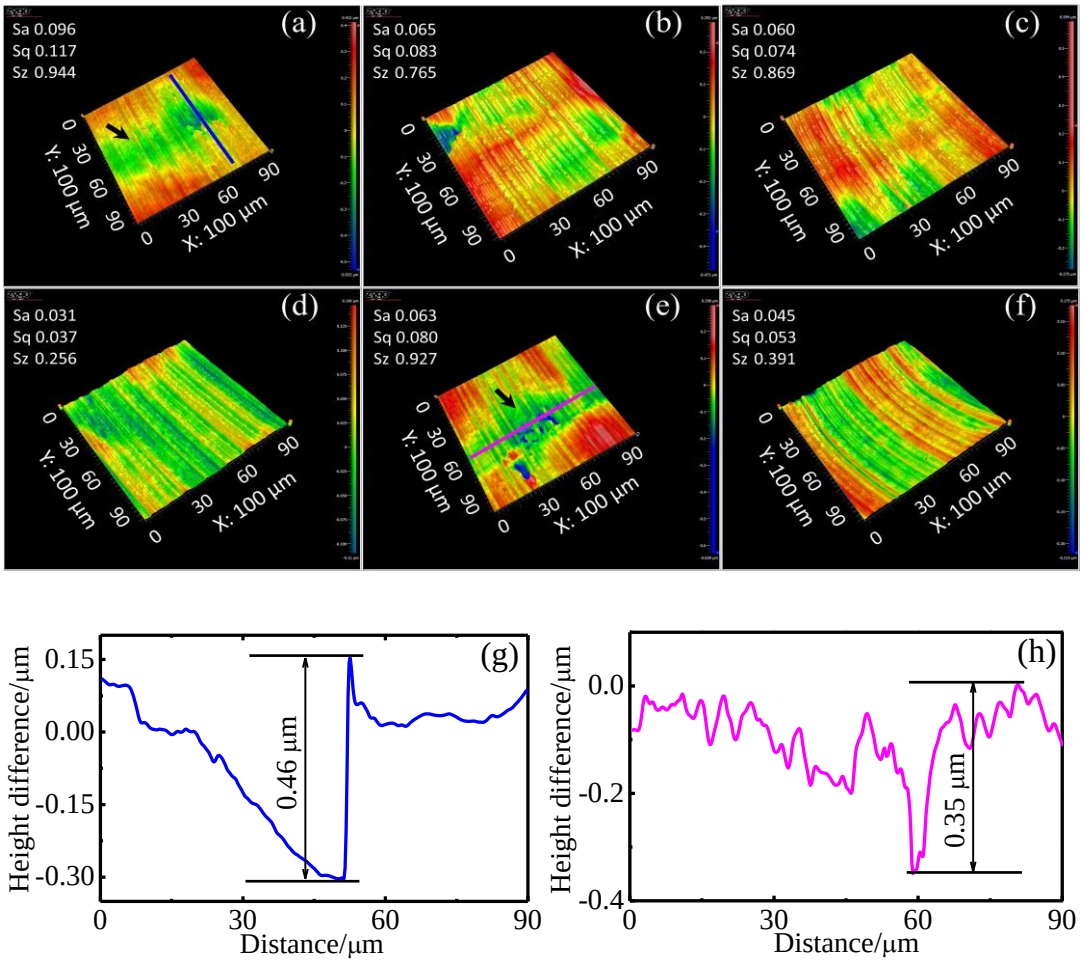

Fig. 5 Zygo profiles of (a)-(c) as received CP Ti and (d)-(f) CEPT specimen; (g) and (h) are the height difference of line 1 and line 2 marked with blue and violet line in (a) and (e), respectively.

3.2 Deformation twin type

Fig. 6 illustrates the inverse pole figure (IPF) orientation mapping of the as-received and CEPT samples. The grain distribution of the original CP Ti is shown in Fig. 6 (a), which is similar to the OM morphology. While the average grain size reduces to about 15 µm at Zone I of CEPT CP Ti and no twins and subgrains are discovered in this zone due to the annealing effect of EPT, as shown in Fig. 6 (b). Besides, a considerable amount of deformation twins of $\{10\bar{1}2\} < 10\bar{1}\bar{1} >$ type (T1 twin) are observed from

Fig. 6 (c) and (d) in Zone II, and the density of twins gradually reduces as the distance decreases from the centre of the samples. Furthermore, the misorientation angle is about 85° deviated from the direction of $< 10\bar{2}0 >$, as illustrated in the point-to-point and point-to-origin curves given in Fig. 6 (f) and (g).

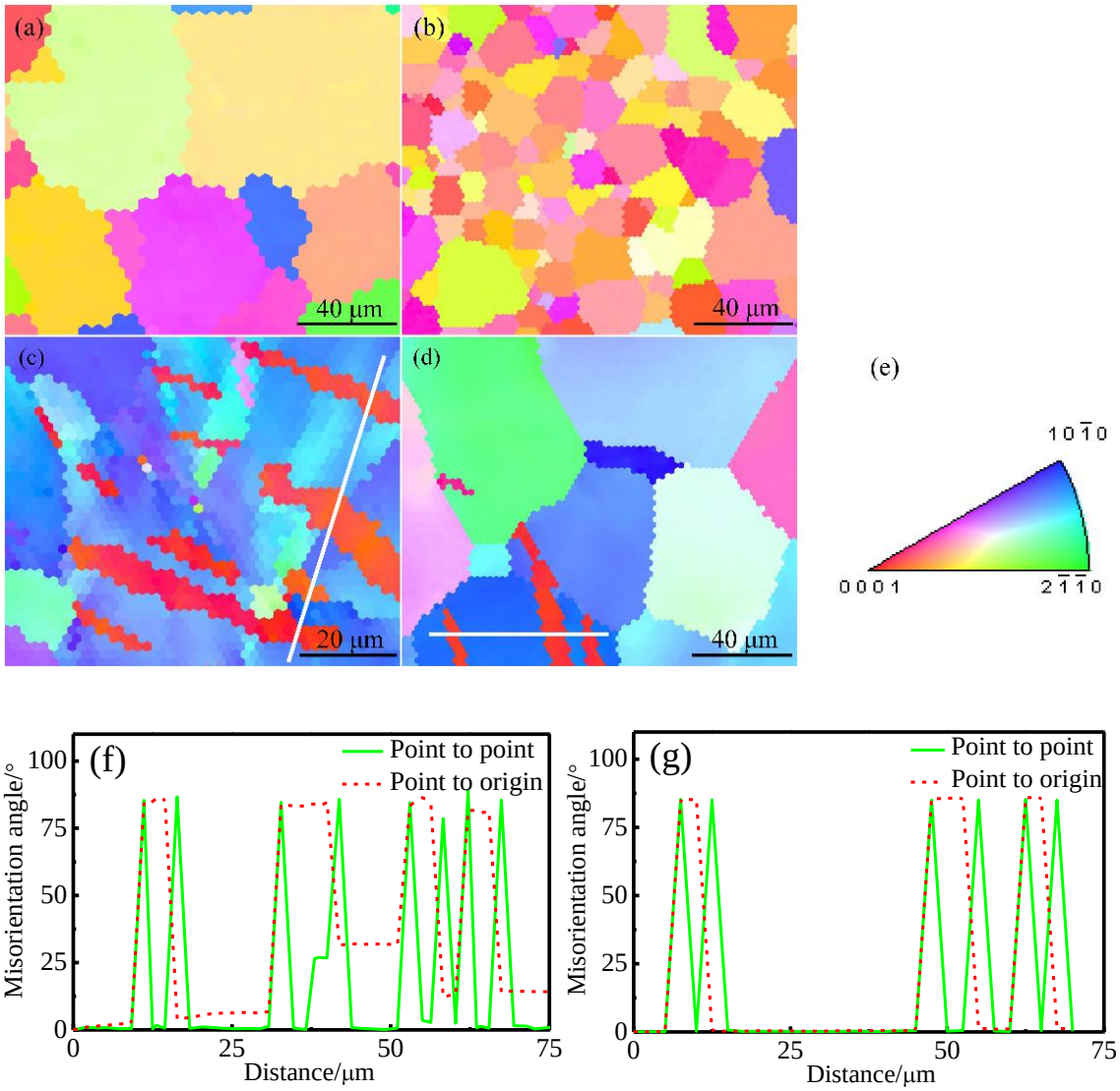

Fig. 6 IPF maps of (a) as received, (b) Zone I, (c) initial site of Zone II and (d) inner site of Zone II; (f) and (g) are the misorientation angle profiles corresponding to the white lines marked in (c) and (d), respectively.

3.3 Microhardness and Youngs modulus

Vikers hardness and Youngs modulus evolution along a diametral direction are given in Fig. 7. The microhardness of the as-received samples fluctuates from 195 HV to 205 HV and the average calculated value is about 199.5 HV. The microhardness evolution in the CEPT treated samples show a symmetrical characteristic due to the symmetrical microstructure of the samples. It can be seen from Fig. 7 (a) that the microhardness reaches the highest value of about 232 HV at the region with small grains. After that, it decreases suddenly to about 203 HV in the region with coarsen crystals and deformation twins. Then, the hardness reduces slightly with the decreasing distance from workpiece centre. A minimum microhardness (about 180 HV) is obtained in the centre of the workpiece with large crystals. Although the regional microhardness of small grains is higher than that of high density twins, the average cutting forces are almost equal to each other. This is caused by the different deformation mechanisms of hardness indentation test and diamond turning process. A similar evolution trend is found in the Young's modulus curves shown in Fig. 7 (b). The maximum value of Young's modulus of the CEPT treated samples is about 124 Gpa, which increases by about 13.8% in comparison with the as-received CP Ti. The enhancement of Young's modulus could contribute to the reduction of inherent spring back, so the rubbing effect between cutting edge and workpiece could be reduced during cutting of titanium and its alloys. This could also contribute to the fine surface quality of the zone with small grains.

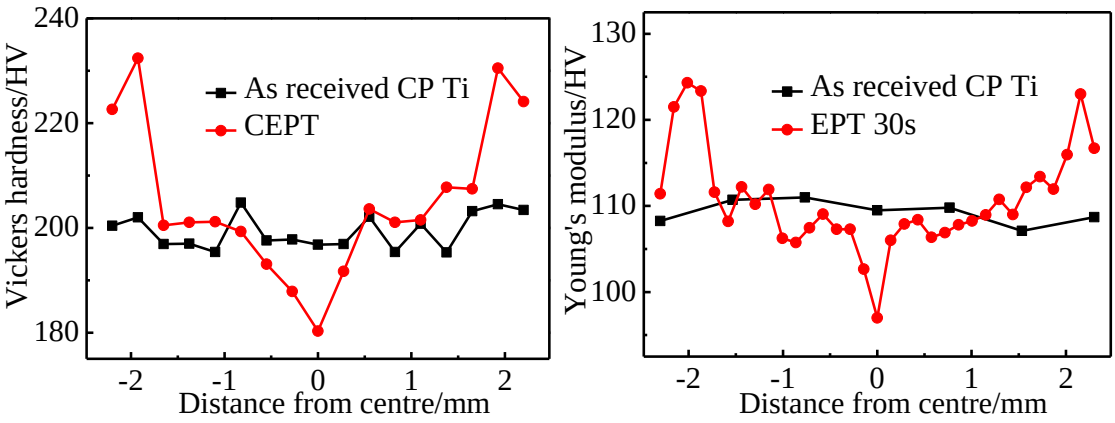

Fig. 7 Evolution of (a) Vickers hardness and (b) Young's modulus

3.4 Cutting forces

Fig. 8 illustrates the main cutting forces variation of the two types of samples during the turning process, and the red smooth lines are obtained by adjacent-averaging method. The vibration amplitudes of both cutting forces are considerably large at the beginning of the curves due to the diamond tool not fully feeding into the samples. Then, the average cutting force of the as received samples shows a slight downward trend with the tool further moving forward into samples (Fig. 8 (a)), while that in CEPT treated samples increases slightly at first and then decreases slowly with the tool feeding into the workpiece, as shown in Fig. 8 (b).

Even though the grain size in the outside of the CEPT treated workpiece is much smaller than that in the as-received one, the average measured cutting forces of them are almost same. This is inconsistent with the well-known Hall-Petch relationship that demonstrates that the yield stress will increase as the grain size decreases. This is because the cutting forces are not only affected by the grain size (grain boundaries), but also correlated to the dislocations and cutting geometries. At the region with small grains, increase in Vikers hardness and Young's modulus in comparison to the as-

received samples demonstrates that the required stress to overcome plastic deformation does enhanced, but the cutting force is also closely affected by the shear angle φ in diamond turning process. Even though a high yield stress is required to overcome deformation, the corresponding cutting forces may not be high due to the large shear angle. This will be discussed in the following section.

It should also be noted that the turning point (black arrow) of cutting force in Fig. 8 (b) corresponds to the emergence of deformation twins presented in Fig. 2 (e), which gives rise to high cutting force vibration. As proposed by Knezevic et al. (2010), the nucleation of twins in hcp metals could result in a new crystal orientation with respect to the parent crystal, and if the re-orientated crystal lattice is in a hard orientation, the material strength and ductility could be enhanced significantly. According to Knezevic et al. (2010), the formation of T1 twins $\{10\bar{1}2\} < 10\bar{1}\bar{1} >$ generally re-orients the grains into hard orientations, resulting in a hardening effect. Besides, Kaschner et al. (2007) demonstrated that the formation of twins in hcp materials hinders the propagation of dislocations, and has a great influence on the strength of hcp crystals because of the dislocation barrier effects. Consequently, the force fluctuation in zone with high density of T1 twins is obvious in comparison to other regions of the CEPT treated workpiece.

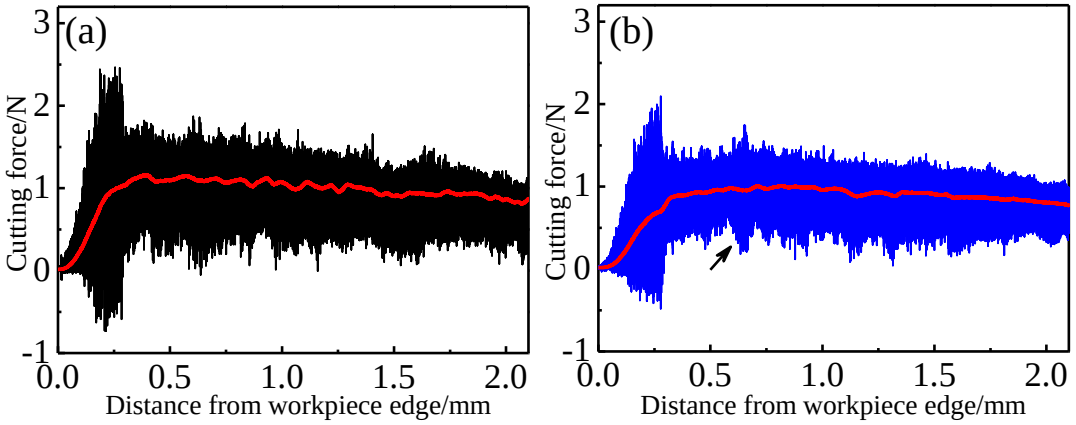

Fig. 8 Main cutting forces of (a) as-received and (b) CEPT treated samples

In order to confirm the effects of deformation twins on cutting force vibration, groove cutting from outside to centre of workpiece with a spindle speed of 60 rpm and cutting depth of 4 μm was conducted. Fig. 9 (a) shows an example of five cutting grooves on one of CEPT treated specimens. Cutting force variations of the as-received and CEPT treated workpiece are shown in Fig. 9 (b) and (c), respectively. For the as-received one, the cutting force of the second groove is smaller than that of the first groove, which is consistent with the force reduction in continuous turning process. However, the cutting force of the second groove where the microstructure is consisted of high density of twins is slightly higher than that of the first groove where microstructure is small grains for the CEPT treated sample. This is also in accordance to the force variation of workpiece with continuous diamond turning.

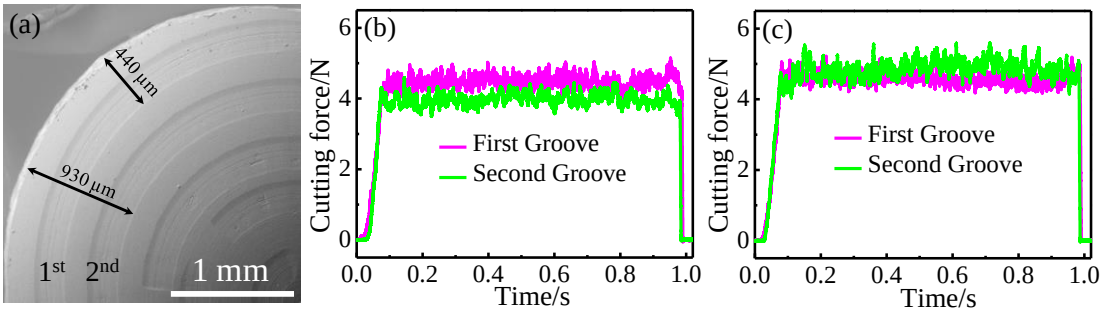

Fig. 9 (a) Groove morphologies, and the first and second cutting forces of (b) as-received and (c) CEPT treated samples

4. Discussion

4.1 Cracks formation

The strength and ductility of alloys are highly affected by grain or twin size. It is widely recognized that decrease in grains or twins could increase the total grain boundary area, which provides a potential to enhance the material strength. Besides, alloys with large grain boundary area have high resistant to crack nucleation by reducing the stress concentration on unit per unit volume of grain boundary according to Vinogradov (2007) and Sangid (2013). In the diamond turning process, the material removal rate is same in the two regions due to the some cutting tool, depth of cut and feed rate. However, as the grain sizes in the outside region is much smaller than those in the internal, the numbers of grain boundaries are different during material removal process, as schematically shown in Fig. 10. The arc length of the material removal edge is calculated to be about 85 μm from the tool geometry, so there are about 6 grains contained in the removal part at the region with grain size of about 15 μm, while at most 2 grains are included in the removal part at grain size ranging from 60 to 100 μm. Small grain size could increase the areas of grain boundary acting as barrier for dislocation movement, so the stress concentration on per unit volume of grain boundary is less under almost same cutting force, which significantly retards crack nucleation at the grain boundaries during turning process.

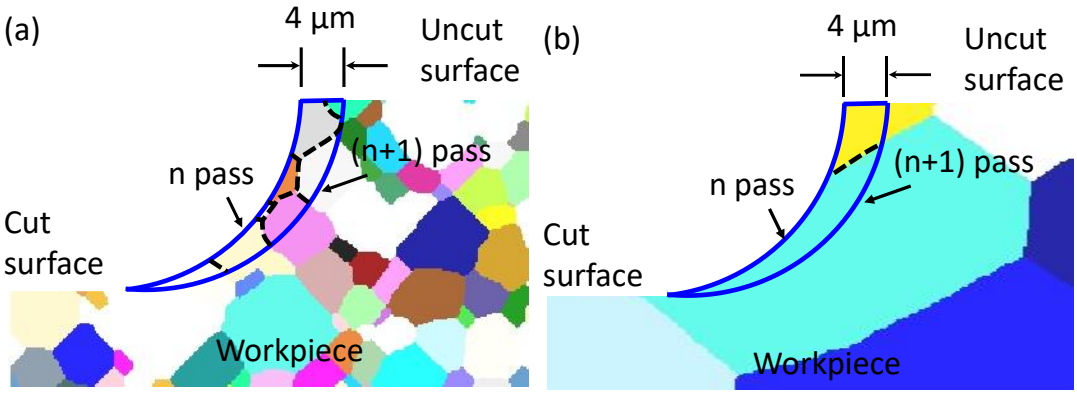

Fig. 10 Schematic diagrams of material removal process of workpiece with grain size of about (a) 15 µm and (b) more than 40 µm. The boundaries in the removal part are marked by black dash lines.

Besides, CP Ti with an average grain size of about 12 µm was obtained via pre-compression (60 % of thickness reduction) followed by EPT of 30 s, as shown in Fig. 11 (c). Then, diamond turning with same cutting parameters in Section 2 was conducted on the workpiece. The numbers of cracks are significantly reduced in comparison to the workpiece with gain size of more than 40 µm, and the average area surface roughness and peak-to-valley value could respectively reduce to about 15 nm and 136.5 nm, as shown in Fig. 11 (a) - (b). Fig. 11 (d) compares the flat mirror surface of the CEPT treated alloy (Workpiece 1) and that with a grain size of 12 µm (Workpiece 2). The reflection quality of the outside region is much better than the internal region for the CEPT treated samples, while that with grain size of 12 µm shows a fine reflection feature throughout the whole surface. Therefore, reduction in grain size could retard crack formation and has potential benefits for improving the surface quality of CP Ti.

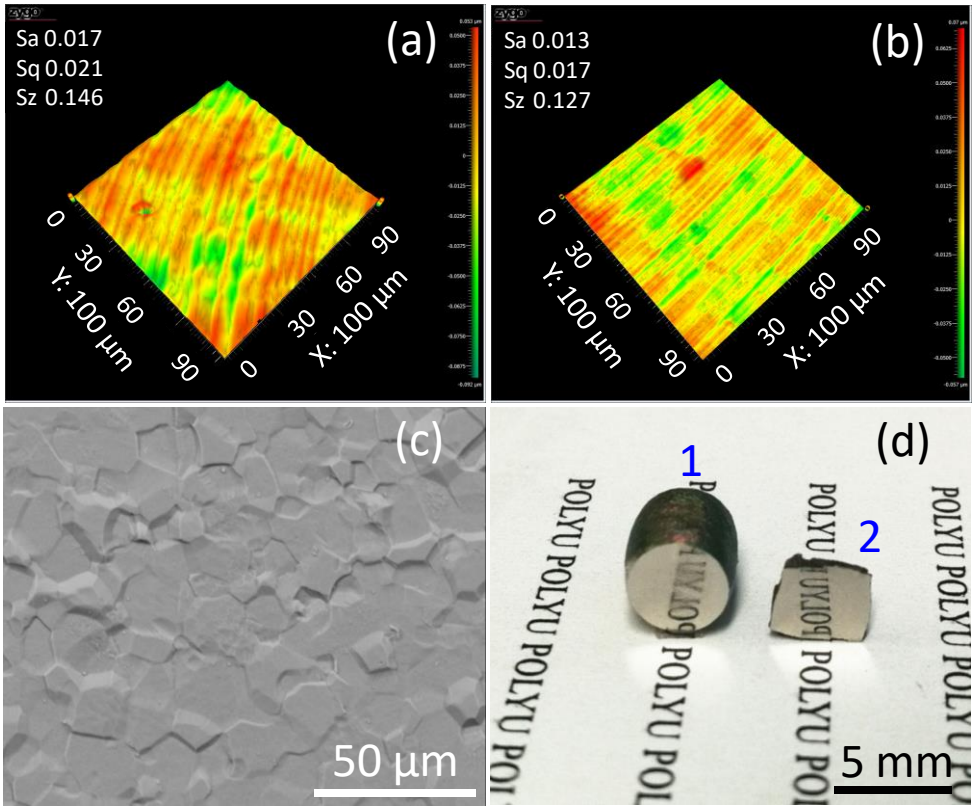

Fig. 11 (a) - (b) Zygo surface topographies of (c) workpiece 2 with an average grain size of about 12 µm and (d) comparison of mirror reflection of two kinds of workpiece

4.2 Deformation models

4.2.1 Flow stress model

Plastic deformation occurs only when the applied stress is higher than the flow stress of cutting layers of CP Ti alloys in ultraprecision diamond turning. In order to achieve plastic deformation of polycrystalline crystals, the applied stress should overcome the critical resolved shear stress (CRSS) τ_c as well as an internal stress τ_r caused by the coupling function of grain boundaries, dislocations and secondary phase particles. Hence, the applied stress τ for activation of plastic deformation can be given by (Melkote et al., 2015):

$$\tau = \tau_{cj} + \tau_i \tag{2}$$

The value of $\tau_{c,j}$ highly depends on the crystal orientation of CP Ti, because the CRSS varies significantly with different glide modes *j* of deformation mechanism. The internal stresses τ_i is induced by two parts in the diamond turning process, i.e. internal resistance stress τ_r and dislocation drag stress τ_d under deformation with a high strain rate. Thus,

$$\tau_i = \tau_r + \tau_d \tag{3}$$

where τ_r is calculated as the total stresses required to conquer the dislocation movement of grain boundaries τ_g, spatially random dislocation forests τ_ρ and patterned distribution of subgrain boundary dislocations τ_{sub}, as follow (Ardeljan et al., 2014):

$$\tau_r = \tau_g + \tau_\rho + \tau_{sub} = \frac{\alpha_g \mu\sqrt{b}}{\sqrt{D}} + \alpha_\rho \mu b\sqrt{\rho} + k_{sub}\mu b\sqrt{\rho_{sub}}\log\left(\frac{1}{b\sqrt{\rho_{sub}}}\right) \tag{4}$$

where α_g and α_ρ are constants that depend on the strength of grain or twin boundaries and dislocation forests, respectively. Shear modulus μ is a temperature dependent parameter, *b* is the magnitude of the Burgers vector, and *D* is the value of average grain/twin size. The dislocation density ρ is closely correlated with the slip-induced hardening and dynamic recovery process. When twins are presented in parent grains, the boundary barrier effect $\tau_{g,twin}$ is expressed by (Knezevic et al., 2015):

$$\tau_{g,twin} = \frac{f^{pts} - f^{pts,0}}{f^{pts,max} - f^{pts,0}} \frac{\alpha_g \mu\sqrt{b}}{\sqrt{D^s_{mfp}}} \tag{5}$$

where $f^{pts,0}$ and $f^{pts,max}$ are constants, representing the minimum and maximum volume fraction of predominant twin system (PTS) of twins in one grain, respectively. The term of D^s_{mfp} denotes the mean-free-path distance and is obtained as follow:

$$D_{mfp}^{s} = \frac{(1-f^{pts)}D_c}{sin\,(\alpha)} \tag{6}$$

where α is an angle between the PTS plane and slip or twin plane of the deformation system, D_c is the distance between twin lamellae:

$$D_c = \frac{D}{n^{lamellae}} \tag{7}$$

where $n^{lamellae}$ represents the number of twin lamellae inside the parent gains. The value of $f^{pts,0}$, $f^{pts,max}$, α, D and $n^{lamellae}$ could be obtained from the experimental results.

The drag stress τ_d that could give rise to a drag pressure on the movement of dislocations under high strain (10^3 s^{-1}) rate deformation can be formulated by:

$$\tau_d = \alpha_d \dot{\varepsilon} \tag{8}$$

where α_d is the dislocation drag coefficient and $\dot{\varepsilon}$ is strain rate during the diamond turning process. Therefore, the final formula to evaluate the applied stress of microstructure with grains and twins can be expressed by:

$$\begin{cases} \tau_{grain} = \tau_{c,grain} + \frac{\alpha_g \mu\sqrt{b}}{\sqrt{D_I}} + \alpha_\rho \mu b\sqrt{\rho_{grain}} + k_{sub}\mu b\sqrt{\rho_{sub}}\log\left(\frac{1}{b\sqrt{\rho_{sub}}}\right) + \alpha_d\dot{\varepsilon} \\ \tau_{twin} = \tau_{c,twin} + \frac{f^{pts}-f^{pts,0}}{f^{pts,max}-f^{pts,0}} \frac{\alpha_g \mu\sqrt{b}}{\sqrt{\frac{(1-f^{pts)}D_{II}}{n^{lamellae}\sin\,(\alpha)}}} + \alpha_\rho \mu b\sqrt{\rho_{twin}} + k_{sub}\mu b\sqrt{\rho_{sub}}\log\left(\frac{1}{b\sqrt{\rho_{sub}}}\right) + \alpha_d\dot{\varepsilon} \end{cases} \tag{9}$$

For CP Ti with hcp crystal structure, the required applied stress to overcome flow stress can be evaluated from equation (9), which considers the effects of crystalline orientations, twins, dislocations and high strain rate during the ultraprecision diamond turning process.

4.2.2 Flow stress model calculation

A considerable amount of work has been conducted to investigate the CRSS of different slip systems of CP titanium. The relevant CRSS values are tabulated in Table 2 and other parameters are listed in Table 3.

Table 2 The relevant literature studies of CRSS values for diverse slip models and extension T1 twin of CP Ti

Pris <a> slip (MPa)	Basal <a> slip (MPa)	Pyr <a> slip (MPa)	Pyr <c+a> slip (MPa)	T1 twin (MPa)	Ref.
60	120	N/A	180	125	(Yang et al., 2011)
80	90	110	260	220	(Warwick et al., 2012)
68	175	120	250	230	(Gloaguen et al., 2013)
96±18	127±33	N/A	≥240	225	(Wang et al., 2017)

Table 3 Parameters from relevant references and present work

Parameters	Value	Ref.
α_g	0.4544	(Melkote et al., 2015)
α_ρ	0.5	(Melkote et al., 2015)
α_d(kPa s)	4.5	(Wulf, 1979)
μ(GPa)	48.66-0.032223T	(Melkote et al., 2015)
b(m^{-1})	2.95×10^{-10}	(Britton et al., 2010)
k_{sub}	0.086	(Capolungo et al., 2009)
D_I(μm)	15	Present work
D_{II}(μm)	90	Present work
$f^{pts,0}$	~0.02	Present work
$f^{pts,max}$	~0.7	Present work

Firstly, we consider the applied stress required in the region with deformation twins in Zone II. As the friction of deformation twins, number of twin lamellas, and dislocation density are simultaneously decreasing in this region, as shown in Fig. 12, we know from equation (9) that the corresponding applied stress should also be decreasing. This is in accordance with the evolution of primary cutting force in ultraprecision machining.

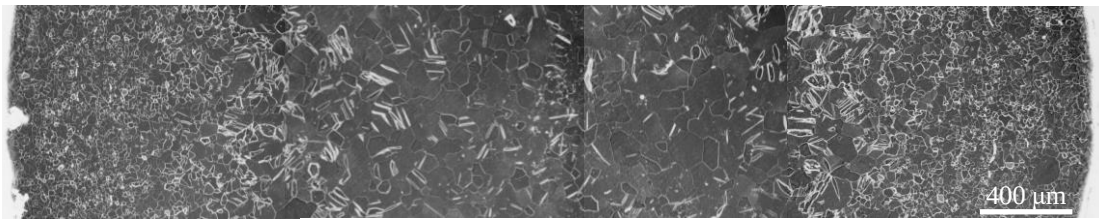

Fig. 12 Whole microstructure of one of CEPT treated samples

Besides, the barrier stress caused by twin and dislocations also significantly affects the applied stress required to plastic deformation. For example, the average numbers of twin lamellas and twin frictions at some beginning sites of Zone II are respectively about 3 and 0.29, as shown in Fig. 13 (a). The relationship between barrier stresses $(\tau_{g,twin} + \tau_{\rho} + \tau_{sub})$ with cutting temperature T and dislocation densities of ρ_{twin}, ρ_{sub} can be obtained from equation (3) - (7), as shown in Fig. 13 (c) - (f). The colour bar shown in the right of each 3D morphology gives the total barrier stress legend. The barrier stress is significantly affected by temperature and dislocation densities, and it is even higher at the region with a high twin density, as shown in Fig. 13 (b). Furthermore, if the extension T1 twin is activated in the turning of Zone II, the value of $\tau_{g,twin}$ equals to 0 Mpa due to the same PTS and activated plane, so the barrier stress is only the sum of stresses required to overcome spatially random dislocation forests τ_{ρ} and subgrain boundary dislocations τ_{sub}, as shown in Fig. 13 (f).

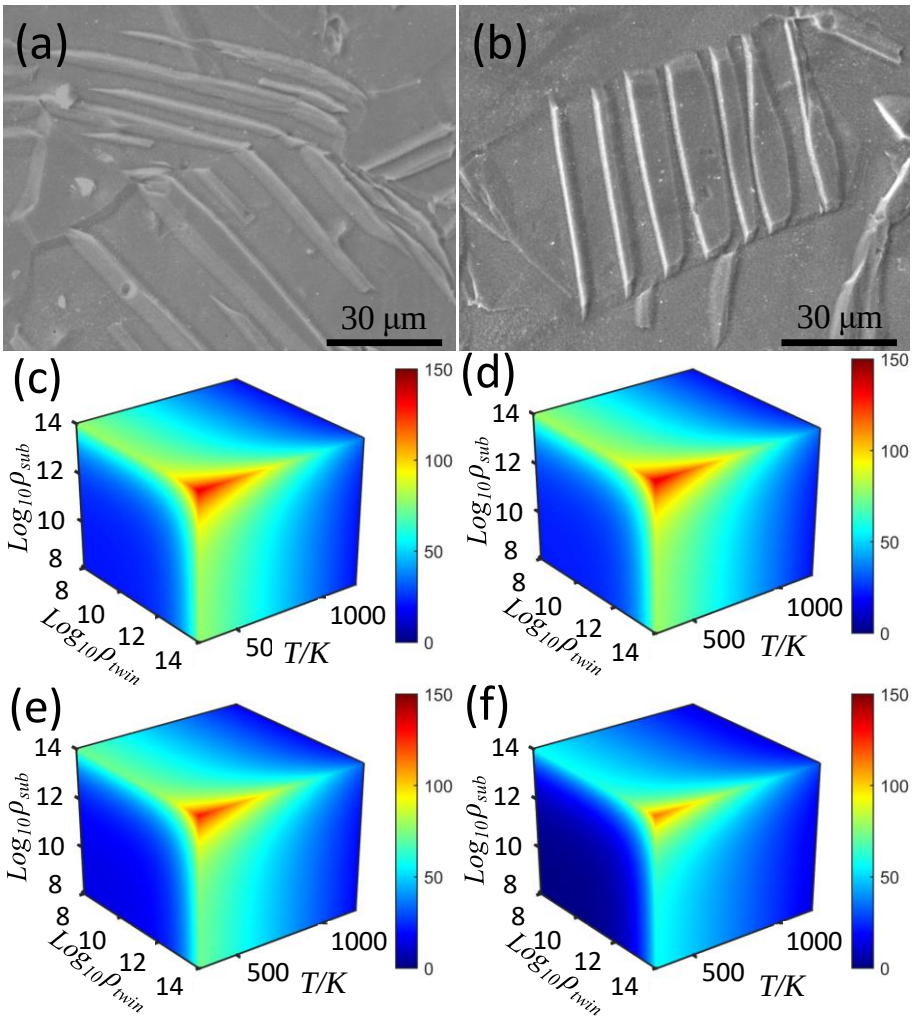

Fig. 13 (a) and (b) are SEM morphologies of twins at two sites of Zone II. Barrier stress distribution varies with cutting temperature and dislocation densities for (c) prismatic <a> slip at α=47.50°, (d) basal <a> slip at α=42.50°, (e) pyramidal <a> slip at α=18.88° and (f) T1 twin at α=0°.

From the main cutting force evolution curve, we know that the average cutting force in Zone I with small grain size almost equals to that in the beginning site of Zone II with relatively high density of deformation twins, so the applied stress of τ_{grain} and τ_{twin} are nearly the same. Besides, grains are fully recrystallized in Zone I and no subgrains or twins are observed in this region from the EBSD map. A reasonable dislocation density of 10^{12} m^{-2} is considered in Zone I after proper annealing treatment by EPT. The barrier

stress of subgrain boundary dislocation is omitted because of the absence of subgrains. Hence, the difference between the CRSS of $\tau_{c,grain}$ in Zone I and $\tau_{c,twin}$ in Zone II can be acquired from equation (9):

$$\tau_{c,grain} - \tau_{c,twin} = \frac{f^{pts} - f^{pts,0}}{f^{pts,max} - f^{pts,0}} \frac{\alpha_g \mu \sqrt{b}}{\sqrt{\frac{(1-f^{pts})D_{II}}{n^{lamellae} sin(\alpha)}}} + \alpha_\rho \mu b \sqrt{\rho_{twin}} +$$

$$k_{sub} \mu b \sqrt{\rho_{sub}}\, log\left(\frac{1}{b\sqrt{\rho_{sub}}}\right) - \frac{\alpha_g \mu \sqrt{b}}{\sqrt{D_I}} - \alpha_\rho \mu b \sqrt{\rho_{grain}}. \quad (10)$$

At the initial site of Zone II, where grains are under modest deformation but not fully recrystallized due to the limit time of EPT, some distorted microstructures could still be observed in this region, so the dislocation densities of ρ_{twin} and ρ_{sub} were assumed to be about 10^{14} m^{-2}. The same twin friction f^{pts} and numbers of twin lamellae $n^{lamellae}$shown in Fig. 13 (a) are utilized to calculate the stress. The relationship of stress difference of CRSS can be simulated as a function of temperature, as shown in Fig. 14. Increase in temperature reduces the CRSS difference of the two Zones. It is generally recognized that the CRSS for prismatic <a> slip is the smallest among the deformation modes of CP Ti with hcp structure, so this slip is believed to be the most likely to be activated in deformation process. However, the prismatic <a> slip is not considered to be the unique deformation mode in Zone I, because the CRSS difference in the two zones is consistently positive (CRSS of Zone I is higher than that of Zone II). Similarly, the pyramidal <c+a> slip with the highest CRSS should be only one of the deformation mechanisms or may not be activated in the beginning site of Zone II.

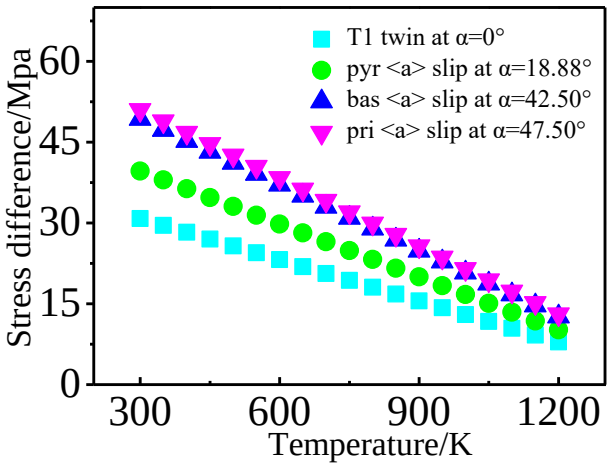

Fig. 14 Evolution of CRSS difference of various deformation modes with temperature between Zone I and the initial site of Zone II

4.2.3 CRSS and cutting shear angle relationship

The applied shear stress τ required to overcome flow stress during diamond turning can be formulated by a ratio between the resultant force along cutting shear plane and the plane area A_s, as follows:

$$\tau = \frac{F_c cos\varphi - F_f sin\varphi}{A_s} \tag{11}$$

where F_c is the main cutting force, F_f is the thrust force and φ is the cutting shear angle. The shear plane area A_s is estimated from Fig. 15, and the value is obtained from:

$$A_s = \frac{d_c}{sin\varphi} l_{AB} \tag{12}$$

where d_c and R are the cutting depth and diamond tool radius respectively. The average length of l_{AB} is measured from the serrated chips after diamond turning, as shown in Fig. 15 (c) and (d). The observation of serrated chips also demonstrates that the workpiece was removed by cutting instead of ploughing. According to equation (9), (11) and (12),

the resolved shear stress required to activate the slips or twins in Zone I with relatively small grains can be expressed by:

$$\tau'_{c,grain} = \frac{F_c cos\varphi - F_f sin\varphi}{\frac{d_c}{sin\varphi} l_{AB}} - \frac{\alpha_g \mu \sqrt{b}}{\sqrt{D_I}} - \alpha_\rho \mu b \sqrt{\rho_{grain}} - \alpha_d \dot{\varepsilon} \quad (13)$$

If the resolved shear stress $\tau'_{c,grain}$ exceeds one of the CRSSes of CP Ti, the corresponding slips or twins could be activated instantly. Fig. 16 illustrates the simulated relationship between the resolved shear stresses, shear angles, strain rates and temperatures in the cutting shear plane of Zone I based on equation (13). Not only temperature, but also the shear angle and strain rate that are closely related to cutting speeds have significant influences on the resolved shear stress.

From Table 2, we know that the CRSS of CP Ti is generally in a range from about 60 Mpa to 300 Mpa with respect to deformation modes, which restricts the strain rate smaller than 10^5 s^{-1} in this experimental conditions. Furthermore, the strain rate of diamond turning is generally larger than 10^3 s^{-1}, so shear angles can be changed from 4° to 30°, as shown in Fig. 16 (a). Besides, the shear angle remains quite stable before the strain rate reaches about 10^4 s^{-1}, but the angle changes dramatically after the strain rate is higher than 10^4 s^{-1} in ultraprecision diamond turning.

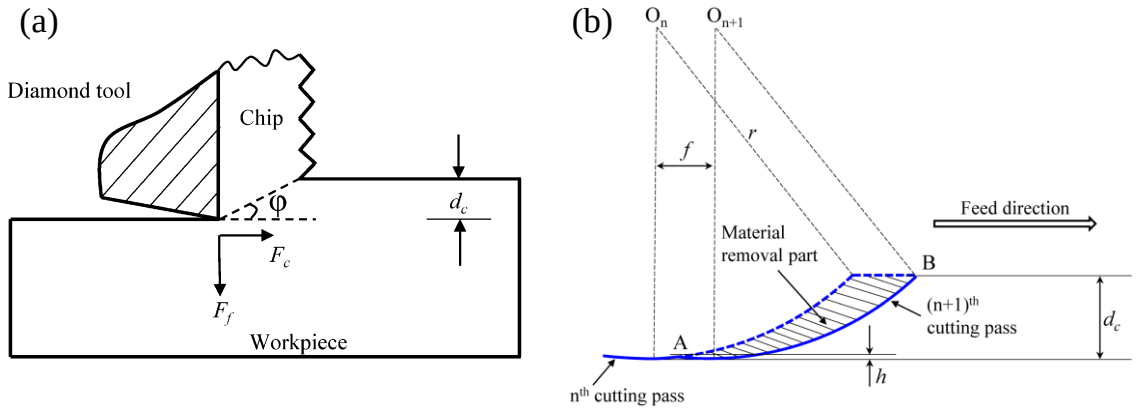

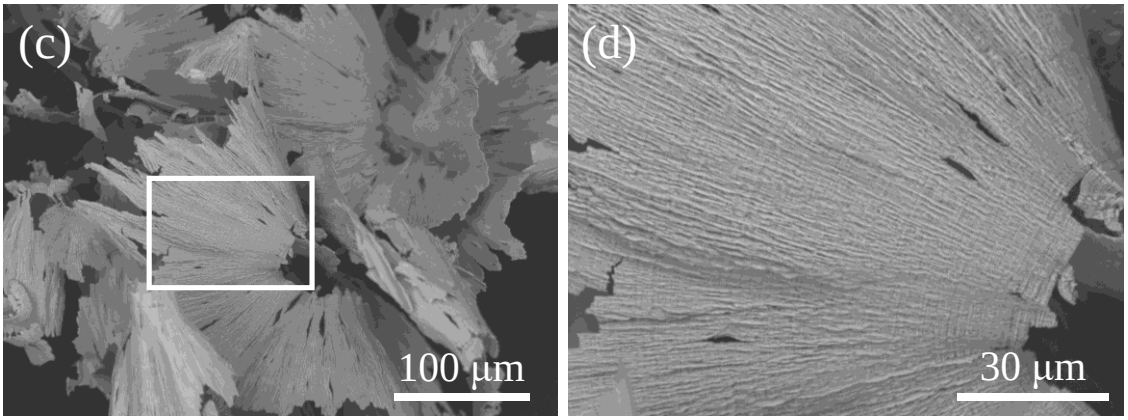

Fig. 15 (A) cross sectional view and (b) front sectional view of material removal process in diamond turning process; (c) chip morphologies after diamond turning of Zone I and (d) a magnifying image of serrated chip marked by white rectangle in (c)

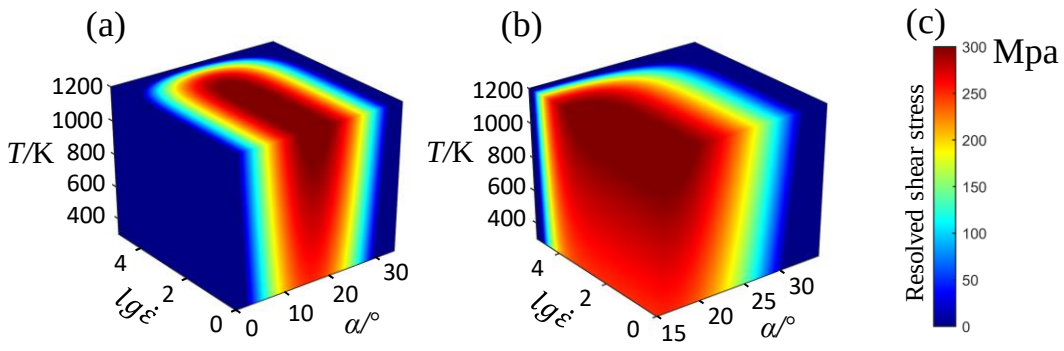

Fig. 16 Simulation relationship of resolved shear stress, strain rate, shear angle and temperature: (a) whole view, (b) cross-sectional view at shear angle of 15° and (c) colour bar

5. Conclusion

The crack nucleation and deformation mechanism of CP Ti have been theoretically and experimentally investigated in ultraprecision diamond turning from perspectives of grain boundaries, resolved shear stresses and barrier stresses, the following conclusions can be drawn.

(1) CP Ti with small grains and deformation twins are respectively obtained in the outer and inner sites of one sample by compression followed by electropulsing treatment for 30 seconds, which provides a desirable microstructure for comparing the effects of grains and twins on the deformation behaviour of CP Ti during ultraprecision diamond turning.

(2) Turning microcracks are mainly observed to be nucleated at large grains and thick twins instead of small grains or twins due to excessive stress concentration on per unit volume of grain boundary. Reduction in grain size could retard crack nucleation and has potential benefits for improving the surface quality of CP Ti.

(3) The CRSS of small grains is larger than that of large grains with a high density of deformation twin of $\{10\bar{1}2\} < 10\bar{1}\bar{1} >$, which means that the deformation mechanism varies with microstructures. As the difference of CRSS between small grains and large grains with twins is consistently positive, the prismatic <a> slip with minimum stress is not the unique deformation mode for small grains; similarly, the pyramidal <c+a> slip with the highest stress should be one of deformation modes or may not be activated for large grains with numerous twins.

(4) The relationship between resolved shear stresses, strain rates, shear angles and temperature is modelled for the first time. From this model, the deformation mechanism in the primary deformation zone of ultraprecision turning can be properly evaluated if the strain rate, shear angle and temperature are given.

Acknowledgments

The work described in this paper was jointly supported by the Research Committee of The Hong Kong Polytechnic University (G-YBLE) and State Key Laboratory of Ultra-precision Machining Technology (RUWB).

References

Allain, S., Chateau, J.-P., Dahmoun, D., Bouaziz, O., 2004. Modeling of mechanical twinning in a high manganese content austenitic steel. Mat. Sci. Eng. A. 387, 272-276.

Ardeljan, M., Beyerlein, I.J., Knezevic, M., 2014. A dislocation density based crystal plasticity finite element model: application to a two-phase polycrystalline HCP/BCC composites. J. Mech. Phys. Solids. 66, 16-31.

Arrazola, P.-J., Garay, A., Iriarte, L.-M., Armendia, M., Marya, S., Le Maitre, F., 2009. Machinability of titanium alloys (Ti6Al4V and Ti555. 3). J. Mater. Process. Tech. 209, 2223-2230.

Beyerlein, I., McCabe, R., Tomé, C., 2011. Effect of microstructure on the nucleation of deformation twins in polycrystalline high-purity magnesium: a multi-scale modeling study. J. Mech. Phys. Solids. 59, 988-1003.

Britton, T., Liang, H., Dunne, F., Wilkinson, A., 2010. The effect of crystal orientation on the indentation response of commercially pure titanium: experiments and simulations, Proceedings of the Royal Society of London A: Mathematical, Physical and Engineering Sciences. The Royal Society, pp. 695-719.

Capolungo, L., Beyerlein, I., Tomé, C., 2009. Slip-assisted twin growth in hexagonal close-packed metals. Scripta. Mater. 60, 32-35.

Cheung, C., Lee, W., 2000. Study of factors affecting the surface quality in ultra-precision diamond turning. Mater. Manuf. Process. 15, 481-502.

Elias, C.N., Lima, J.H.C., Valiev, R., Meyers, M.A., 2008. Biomedical applications of titanium and its alloys. JOM. 60, 46-49.

Furukawa, Y., Moronuki, N., 1988. Effect of material properties on ultra precise cutting processes. Cirp Ann-Manuf. Techn. 37, 113-116.

Gloaguen, D., Oum, G., Legrand, V., Fajoui, J., Branchu, S., 2013. Experimental and theoretical studies of intergranular strain in an alpha titanium alloy during plastic deformation. Aata. Mater. 61, 5779-5790.

Gumus, B., Bal, B., Gerstein, G., Canadinc, D., Maier, H., Guner, F., Elmadagli, M., 2015. Twinning activities in high-Mn austenitic steels under high-velocity compressive loading. Mat. Sci. Eng. A. 648, 104-112.

Hutchinson, W., Barnett, M., 2010. Effective values of critical resolved shear stress for slip in polycrystalline magnesium and other hcp metals. Scripta. Mater. 63, 737-740.

Kaschner, G., Tomé, C., McCabe, R., Misra, A., Vogel, S., Brown, D., 2007. Exploring the dislocation/twin interactions in zirconium. Mat. Sci. Eng. A. 463, 122-127.

Knezevic, M., Levinson, A., Harris, R., Mishra, R.K., Doherty, R.D., Kalidindi, S.R., 2010. Deformation twinning in AZ31: influence on strain hardening and texture evolution. Aata. Mater. 58, 6230-6242.

Knezevic, M., Zecevic, M., Beyerlein, I.J., Bingert, J.F., McCabe, R.J., 2015. Strain rate and temperature effects on the selection of primary and secondary slip and twinning systems in HCP Zr. Aata. Mater. 88, 55-73.

Kusama, T., Omori, T., Saito, T., Kise, S., Tanaka, T., Araki, Y., Kainuma, R., 2017. Ultra-large single crystals by abnormal grain growth. Nat. Commun. 8, 354.

Lee, W., Wang, H., Chan, C., To, S., 2013. Finite element modelling of shear angle and cutting force variation induced by material anisotropy in ultra-precision diamond turning. Int. J. Mach. Tool. Manu. 75, 82-86.

Melkote, S.N., Liu, R., Fernandez-Zelaia, P., Marusich, T., 2015. A physically based constitutive model for simulation of segmented chip formation in orthogonal cutting of commercially pure titanium. CIRP Ann. 64, 65-68.

Muhammad, R., Hussain, M.S., Maurotto, A., Siemers, C., Roy, A., Silberschmidt, V.V., 2014. Analysis of a free machining α+ β titanium alloy using conventional and ultrasonically assisted turning. J. Mater. Process. Tech. 214, 906-915.

Priarone, P.C., Klocke, F., Faga, M.G., Lung, D., Settineri, L., 2016. Tool life and surface integrity when turning titanium aluminides with PCD tools under conventional wet cutting and cryogenic cooling. Int. J. Adv. Manuf. Tech. 85, 807-816.

Qin, H., Jonas, J.J., 2014. Variant selection during secondary and tertiary twinning in pure titanium. Aata. Mater. 75, 198-211.

Rahman, M.A., Rahman, M., Kumar, A.S., 2017. Modelling of flow stress by correlating the material grain size and chip thickness in ultra-precision machining. Int. J. Mach. Tool. Manu. 123, 57-75.

Sahoo, S., Sabat, R., Sahni, S., Suwas, S., 2016. Texture and microstructure evolution of commercially pure titanium during hot rolling: Role of strain-paths. Mater. Design. 91, 58-71.

Salem, A., Kalidindi, S., Semiatin, S., 2005. Strain hardening due to deformation twinning in α-titanium: Constitutive relations and crystal-plasticity modeling. Aata. Mater. 53, 3495-3502.

Sangid, M.D., 2013. The physics of fatigue crack initiation. Int. J. Fatigue. 57, 58-72.

Sharman, A., Aspinwall, D., Dewes, R., Bowen, P., 2001. Workpiece surface integrity considerations when finish turning gamma titanium aluminide. Wear. 249, 473-481.

Shokrani, A., Dhokia, V., Newman, S.T., 2016. Investigation of the effects of cryogenic machining on surface integrity in CNC end milling of Ti–6Al–4V titanium alloy. J. Manuf. Process. 21, 172-179.

Sun, Q., Guo, Q., Yao, X., Xiao, L., Greer, J.R., Sun, J., 2011. Size effects in strength and plasticity of single-crystalline titanium micropillars with prismatic slip orientation. Scripta. Mater. 65, 473-476.

Ulutan, D., Ozel, T., 2011. Machining induced surface integrity in titanium and nickel alloys: A review. Int. J. Mach. Tool. Manu. 51, 250-280.

Vinogradov, A., 2007. Fatigue limit and crack growth in ultra-fine grain metals produced by severe plastic deformation. J. Mater. Sci. 42, 1797-1808.

Wang, L., Zheng, Z., Phukan, H., Kenesei, P., Park, J.-S., Lind, J., Suter, R., Bieler, T.R., 2017. Direct measurement of critical resolved shear stress of prismatic and basal slip in polycrystalline Ti using high energy X-ray diffraction microscopy. Aata. Mater. 132, 598-610.

Warwick, J., Jones, N., Rahman, K., Dye, D., 2012. Lattice strain evolution during tensile and compressive loading of CP Ti. Aata. Mater. 60, 6720-6731.

Wulf, G., 1979. High strain rate compression of titanium and some titanium alloys. Int. J. Mech. Sci. 21, 713-718.

Xie, C., Fang, Q., Liu, X., Guo, P., Chen, J., Zhang, M., Liu, Y., Rolfe, B., Li, L., 2016. Theoretical study on the $\{1\bar{0}12\}$ deformation twinning and cracking in coarse-grained magnesium alloys. Int. J. Plasticity. 82, 44-61.

Yang, Y., Wang, L., Bieler, T., Eisenlohr, P., Crimp, M., 2011. Quantitative atomic force microscopy characterization and crystal plasticity finite element modeling of heterogeneous deformation in commercial purity titanium. Metall. Mater. Trans. A. 42, 636-644.